Enhancing Microwave Sensor Performance with Ultra-High Q Features Using CycleGAN

Nazli Kazemi, Petr Musilek, *Senior Member, IEEE*

Abstract—In this work, a microwave planar sensor is used for liquid material characterization. Two identical complementary split-ring resonators operating at 3 GHz are coupled to create a highly sensitive capacitive region. The moderate quality factor of the sensor ≈ 230 is significantly improved up to ≈ 5040 with loss compensation using a regenerative amplifier. The moderate quality factor restrains the passive mode sensor from distinguishing low concentrations of $1\%-4\%$ water in ethanol, while considerably distinct profiles are achievable using the active-mode sensor. The measured passive mode sensor response is then processed using CycleGAN, a machine learning algorithm conventionally used for image-to-image translation. This strongly enhances the quality factor of the responses, effectively translating them to the active domain. This improvement reduces the limit of water detection down to 1% for water-in-ethanol mixture. In addition, the sensor is used for noninvasive monitoring of glucose levels, in both passive and active modes. The resolution of the CycleGAN-boosted response approaches that of the active sensor (≈ 20 mg/dL), showing a considerable enhancement when compared to the resolution of the passive sensor (≈ 70 mg/dL).

Index Terms—CycleGAN, machine learning, microwave sensor, loss-compensation, glucose sensing

I. INTRODUCTION

MICROWAVE sensors have several advantages when compared to their optical and electrochemical counterparts. They include portability, small form factor, label-free detection, and most importantly, noncontact sensing. High level of accuracy can be achieved with inexpensive and low-profile designs. Over the past two decades, applications of microwave sensors have been growing in various fields including biosensing [1], [2], food quality monitoring [3], material characterization [4]–[13], environmental monitoring [14]–[20], and monitoring of mechanical motion and strain [21], [22].

Microwave resonator-based sensors are based on the environmental influence on the resonance profile of the sensor [8], [23]. Since planar sensors expose their sensitive regions to the surrounding medium, they are susceptible to ambient variations. The high sensitivity of resonator-based sensors [24] makes them suitable for high-end applications towards replacing conventional and expensive equipment for sensing minute variations. This high sensitivity is obtained when the electromagnetic field generated by the sensor propagates and

interacts with the surrounding medium. While this feature is the main factor allowing noninvasive sensing, it also leads to the loss of power in free space. Most such sensors do not use electronics and act passively. Passive sensors, however, suffer from typical dielectric and ohmic losses, resulting in a moderate quality factor. Consequently, the performance of passive sensors is limited due to low-quality factor resonances. One compelling method to address this concern, elaborated in [1], [25], is to amend the sensor with amplifying electronics to compensate the lost power with a recovering scheme. In this technique, the passive core resonator is embedded in a regenerative amplifier or coupled to a negative resistor that samples the sensor signal at resonance and returns its amplified form with a modified phase towards a constructive summation. The net effect is to remove the loss incurred in various sources. This recently developed platform provides significant performance enhancement in sensitive applications. Such active sensors have a high quality factor which increases the resolution of sensing. Through active design, the quality factor can be increased by orders of magnitude to achieve ultra-high resolution sensing [26]–[29]. However, increasing the electromagnetic wave propagation into free space leaves it more susceptible to undesired external influences, such as material proximity, humidity, and temperature [5], [11], [12], [30], [31]. Therefore, the long-term operation of active sensors is prone to errors and the sensors need to be encapsulated for robust functioning. In addition, the electronics require a continuous power supply. This brings additional challenges that require either the use of bulky batteries or the implementation of wireless powering technology [32].

When adopting low-profile passive structures for highly sensitive applications, the ultra-high quality factor feature of active sensors needs to be retrieved. An important example of high-end sensing application can be found in diabetic care. Normal concentration of glucose in the human body ranges between roughly 70 mg/dL up to around 110 mg/dL when measured after overnight fasting. Higher than 140 mg/dL at 2 hours after a meal is called hyperglycemia, a condition which may cause serious health complications including blindness [9], [33], kidney disease [34], and cardiovascular problems [1], [35]–[37]. Therefore, diabetic patients are used to monitor their blood glucose level regularly with the conventional method of pricking the finger for a blood drop on a test strip of an electrochemical sensor. However, this method is not convenient to be conducted regularly. Moreover, a continuous monitoring scheme could facilitate prediction of near-future trends to trigger preemptive remedial actions.

The concentration of glucose is too low to be determined accurately across several skin layers (see Fig. 1). For this
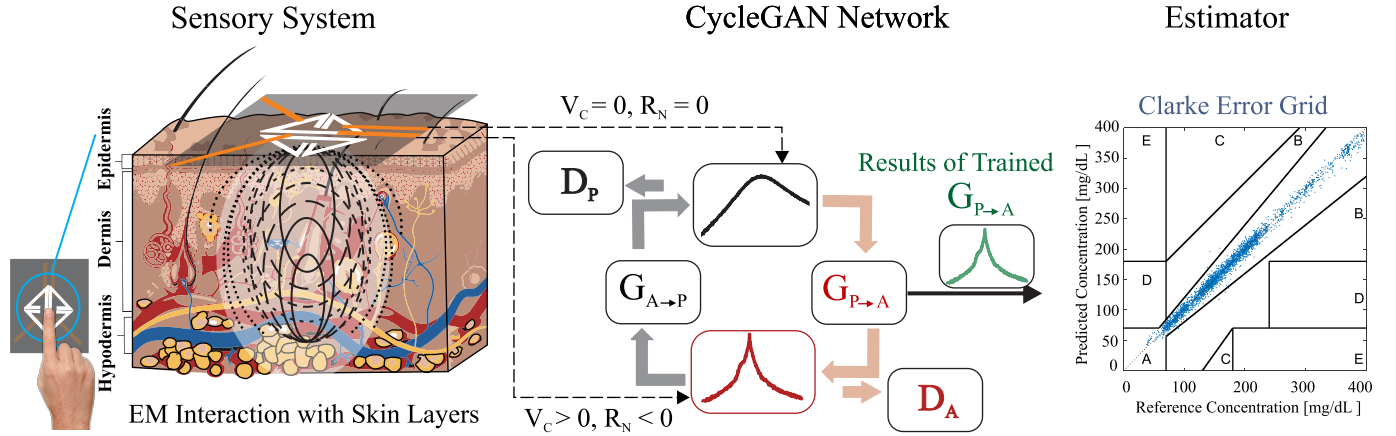
Fig. 1. Microwave sensing scheme combined with CycleGAN network towards improved confusion matrix.

reason, the use of a noninvasive sensor with high resolution is desired, ideally implemented as a wearable device [2], [38], [39].

While developing a high-resolution sensing device is desirable in glucose sensing, recent developments of intelligent systems in microwave engineering [40]–[45] inspires us to adopt a machine learning-based algorithm in this work.

This novel system uses machine learning [46] to provide high resolution response without using power-hungry and error-prone active sensors. It is based on CycleGAN, a technique that learns mapping between two sets of data using unpaired dataset [47], [48]. Applied to sensing, it captures the characteristics of low-to-moderate quality factor profiles from the passive response (passive domain) into meaningfully equivalent high-resolution profiles (active domain), all without the presence of paired training examples. While the passive domain P and the active domain A are distributed identically, there could be many mappings $G : P \mapsto A$ that will result in the same distribution. This is resolved by cycle consistency loss, which ensures that the mapping G is consistent with a reverse mapping $F : A \mapsto P$. Combination of this loss factor with adversarial loss leads to the unpaired passive-to-active mapping (see Fig. 1). We introduce an image representation of the sensor response to exploit machine learning techniques available in the image processing domain. This method retrieves the active sensor performance in the format of an intelligent sensory system based on a passive sensor with an improved accuracy.

II. SENSOR DESIGN

A. Coupled CSRRs

In this work, a planar microwave sensor is designed using metamaterial-inspired inclusions, namely, complementary split ring resonators (CSRRs). These structures are normally etched out of the solid ground to leave a defected ground. Slots are sized to be 0.5 mm thick, which is an achievable accuracy through in-house etching process using ammonium persulfate. The CSRRs have been designed with triangular shape to achieve a high coupling with another similar resonator through capacitive coupling. A pair of CSRRs are placed in 0.5 mm

distance from each other as shown in Fig. 2(a) connected to the active circuit as given in Fig. 2(b). Hereafter, the two resonators lined this way are called coupled CSRRs (CCSRRs). This arrangement is designed to increase the sensitivity of the sensor when the coupled region between two parallel slots is used to interrogate the surrounding material. This feature is shown in Fig. 2(c) with two identical parallel resonators (R, C, and L). These resonators are coupled to each other using capacitive slots represented with equivalent J-inverter configuration given in Fig. 2(c) with coupling capacitor C_m. This coupling between two resonators results in separation of the original resonances to new values as follows:

$$\omega_1 = 1/\sqrt{L(C + C_m)}, \qquad \omega_2 = 1/\sqrt{L(C - C_m)} \quad (1)$$

As a results, the two identically coupled resonators are considered as a new system containing two non-coupled resonators with two different frequencies (ω_1, ω_2), where the modified resonances already contain the coupling information, this allows them to be cascade in the following analysis. The whole design is also coupled to the input/output transmission lines through coupling capacitors C_{TL}.

Another representation of the present network combines two individual back-to-back resonators that are in series. The transfer function representation of each resonator is given as follows:

$$H_1(s) = \frac{K_1 \frac{s\omega_1}{Q_1}}{s^2 + \frac{s\omega_1}{Q_1} + \omega_1^2}, \quad H_2(s) = \frac{K_2 \frac{s\omega_2}{Q_2}}{s^2 + \frac{s\omega_2}{Q_2} + \omega_2^2}, \quad (2)$$

where K_1 and K_2 represent maximum individual transmission amplitude, ω_1 and ω_2 are the resonance frequencies ($s = j\omega$), and Q_1 and Q_2 are the loaded quality factor of each resonator. Upon activating the amplifier of the circuit, the main contributing factors for resonator loss, also known as ohmic loss is compensated. The amplifier in the feedback loop injects extra power in the system in a constructive way, thereby increasing the loaded quality factor. This system can be summarized as follows:

$$H_{total} = \frac{Y(s)}{X(s)} = \frac{H_1(s)H_2(s)}{1 - A_v H_1(s)H_2(s)}, \quad (3)$$
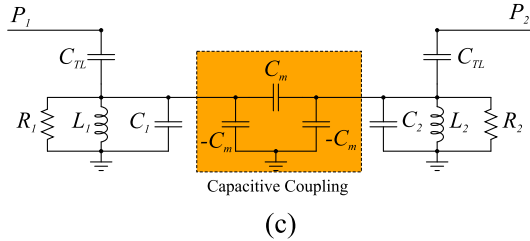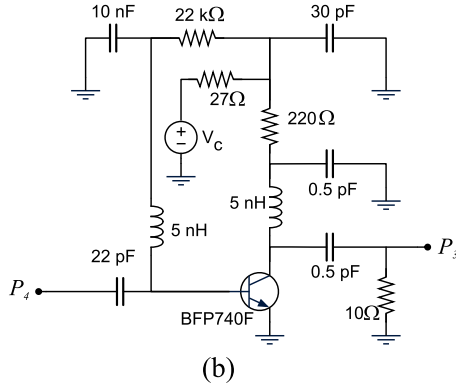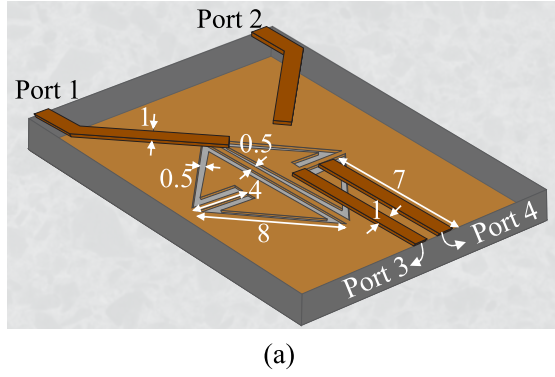
(a)

(b)

(c)

Fig. 2. (a) Schematic of the active CCSRR with corresponding circuit. All dimensions are in [mm], (b) Equivalent circuit model of the passive circuit.

$$H_1(s)H_2(s) = \frac{K_1 \frac{s\omega_1}{Q_1}}{s^2 + \frac{s\omega_1}{Q_1} + \omega_1^2} \times \frac{K_2 \frac{s\omega_2}{Q_2}}{s^2 + \frac{s\omega_2}{Q_2} + \omega_2^2}. \quad (4)$$

where the two coupling capacitors C_{TL} before and after the amplifier A_v are assumed to be included into the amplifier transfer function as elaborated in 3 as these frequency-independent elements act minimally as attenuators preceding and following the amplifier.

It can be shown that if the two original frequencies are close to each other ($\omega_1 \approx \omega_2$):

$$H_1(s)H_2(s) = H_1(s)\underbrace{\frac{\frac{\omega_1}{Q_1}}{\frac{Q_1}{\omega_1} - \frac{Q_2}{\omega_2}}}_{B_1} - H_2(s)\underbrace{\frac{\frac{\omega_2}{Q_2}}{\frac{Q_1}{\omega_1} - \frac{Q_2}{\omega_2}}}_{B_2}, \quad (5)$$

then (3) can be rearranged as:

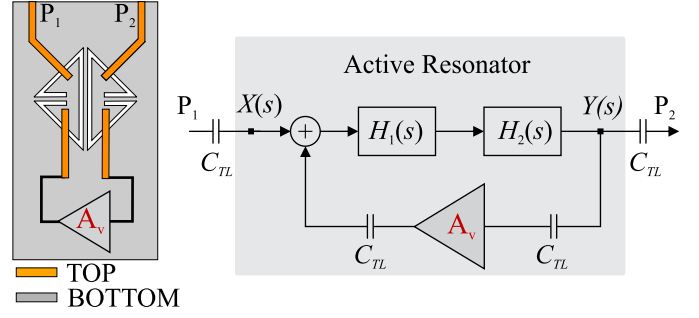$$H_{total} = \frac{B_1 H_1(s) - B_2 H_2(s)}{1 - A_v B_1 H_1(s) - A_v B_2 H_2(s)}. \quad (6)$$

Fig. 3. Equivalent block diagram of the proposed sensor

Assuming that the resonators are identical, then (6) can be simplified considering $\omega_1 \approx \omega_2$, $Q_1 \approx Q_2$, and $K_1 \approx K_2$:

$$H_{total} \approx \frac{B_1 H_1(s) - B_2 H_2(s)}{1 - 2A_v B_1 H_1(s)} \approx \frac{B_1 H_1(s) - B_2 H_2(s)}{1 - 2A_v B_2 H_2(s)}$$
$$= \frac{B_1 H_1(s)}{1 - 2A_v B_1 H_1(s)} - \frac{B_2 H_2(s)}{1 - 2A_v B_1 H_1(s)} \quad (7)$$

Each term in (7) can be simplified as follows:

$$\frac{B_1 H_1(s)}{1 - 2A_v B_1 H_1(s)} = \frac{\frac{B_1 K_1}{1 - 2A_v B_1 K_1} s \frac{\omega_1}{Q_1/(1 - 2A_v B_1)K_1}}{s^2 + s\frac{\omega_1}{Q_{1/(1-2A_v B_1 K_1)}} + \omega_1^2}. \quad (8)$$

This shows that the original resonators' parameters, including amplitude (K_1 and K_2) and loaded quality factor, become amplified by the factor of $((1 - 2A_v B_1 K_1)^{-1})$ or $((1 - 2A_v B_2 K_2)^{-1})$ as follows:

$$K_1 \to \frac{B_1 K_1}{1 - 2A_v B_1 K_1}, \quad Q_1 \to \frac{Q_1}{1 - 2A_v B_1 K_1} \quad (9)$$

This amplification coefficient is controlled by the active circuit, which is triggered using the bias voltage V_C. The principle of operation of the regenerative amplifier relies on two main factors. First, the gain of the system denoted as A_v, must be high enough to compensate the transmission loss of the two series blocks H_1 and H_2. Second, the phase of the signal needs to incur a change of even multiples of 2π so that a positive construction occurs when the present signal in the loop joins the input signal. The signal's phase undergoes a negative sign within the amplifier. For the rest of the phase modification, extra transmission lines are used that connect the core passive resonator to the amplifier. The total length of 35 mm per CSRR, with the dimensions presented in Fig. 2(a), results in dual resonances around 3.5 GHz. The frequency of operation affects the depth of penetration into the free space and sensitivity of the sensor differently. A relatively high frequency is selected to gain more sensitivity [3], [4]. In addition, the size of the resonator is inversely linked to the frequency of operation. Finally, the CSRR edges are folded inwards, similar to the detailed development described in [5], to reduce the overall sensor size and contribute to its miniaturization.

B. Loss Compensation in CCSRRs

Microwave sensors need to have loaded quality factor sufficient to overcome high power loss when exposed to external
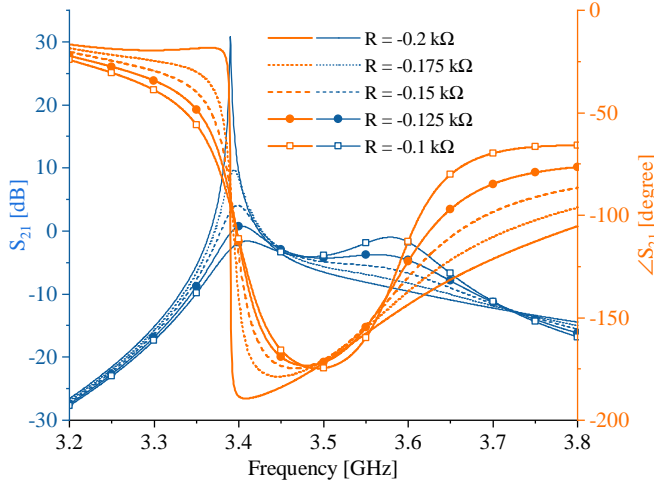
Fig. 4. Simulation results of the CSRR with loss compensation representation in both amplitude and phase of resonance.
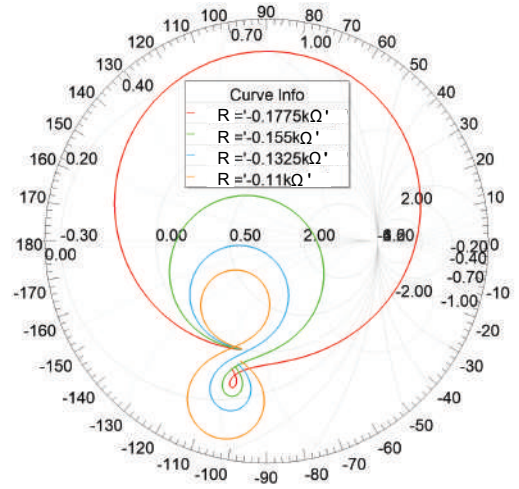

Fig. 5. Smith chart characterization with various loss compensation states.

materials. This inherent challenge has been addressed using various loss-compensating mechanisms, but only for single resonators. However, the proposed system uses a different type of resonator with intrinsic coupling mechanism. Loss-compensation treatment of this CCSRR is implemented using a regenerative amplifier design, as shown in Fig. 3. The input power from port 1 is coupled to the CCSRR and then flows on to the active circuitry through a transmission line. The input power is amplified and phase modified before returning back to the CCSRR for the second time. Once the returned power circulates in the CCSRR, it is sampled through the output transmission line. The phase of amplifier response is controlled to assure constructive feedback in the resonating system. This process also affects the transmission (S_{21}) and reflection (S_{11}) parameters of the sensor. Although the coupled design results in two adjacent resonances, only one resonance is designed to meet the criteria for correct phase compensation. The entire sensor is fabricated on Rogers RO3003 substrate with dielectric properties of $\varepsilon_r = 3.0$ and $\tan(\delta) = 0.0013$. A 0.8 mm substrate holds both the passive resonator design on one side and the active circuitry on the other side. The active circuit is composed of commercially available surface mount electronic devices. Sensor performance with an external loss compensation mechanism is presented in Fig. 4, where both amplitude and phase responses are shown. The simulation model includes a shunt negative resistance in series with a variable phase element from both transmission lines (port 3 and port 4) exiting the CCSRRs to the ground. A fixed phase value of 126° with a variable negative resistance results in the sharpened transmission profiles shown in Fig. 4. The resonance frequency of the sensor changes slightly; however, the loaded quality factor increases significantly. In an initial form of operation in active mode, where the negative resistance is close to -100 Ω, the two resonances yield a very low-resolution profile. The more compensation is applied to the coupled resonators, the sharper the resonance becomes. For this particular example, a typical sharp resonance can be realized with a negative resistance of -200 Ω. The nature of

the coupling between the two resonances causes that only one of them is dominant. In this design, the resonance with lower frequency is set to be dominant. Once the sensor is exposed to a change in the environment, the entire resonance profile shifts downwards. In addition, the resonance frequencies of adjacent resonators are separated from each other as a result of the sensor being exposed to an external material. [49], [50]. Consequently, the net downshift for the lower resonance is higher than that of the upper resonance. The reason for selecting the lower resonance is the ability to exploit its larger resonance dynamics in sensing. The process of loaded quality factor enhancement can also be verified by monitoring the phase information in Fig. 4. It can be seen that the phase diagram for the lower resonance becomes sharper as the negative resistance increases. The well-determined unloaded quality factor Q_0 for the sensor can be computed using the following expression [51]:

$$Q_0 = \frac{f_0}{(f_2 - f_1)\sqrt{1 + \left(\frac{G_0(f_2 - f_1)}{4}\right)^2}}, \qquad (10)$$

where f_0 is the center frequency, characteristic frequencies of f_1 and f_2 are frequencies where phase response has zero slope (excluding frequency-dependent phase contribution from the input/output transmission lines), and the gradient G_0 is the slope of phase at the center frequency. When the negative resistance increases, the quantity $(f_2 - f_1)$ reduces, and that results in an increased loaded quality factor. In this simulated example, the loaded quality factor rises from a nearly passive structure ($R = -100$ Ω) of $Q_0 \approx 15$ up to highly compensated version ($R = -200$ Ω) of $Q_0 \approx 683$. In cases where de-embedding transmission lines' effect becomes ambiguous an alternative solution is to consider the maximum transmission at resonance frequency f_0 ($\max|S_{21}| = S_{21\ 0}$) and the peak width (Δf) at a given level below $S_{21\ 0}$, that is evaluated at $S_{21\ U}$ as follows [52]:

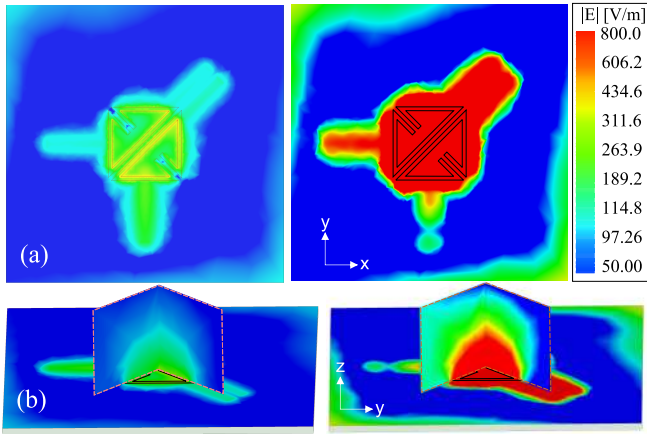$$|S_{21\ U}|^2 = \frac{S_{21\ 0}^2}{S_{21\ 0}^2 - 2S_{21\ 0} + 2} \qquad (11)$$

Fig. 6. Electric Field concentration (a) on the surface and (b) surrounding the sensor in both passive (left) and active (right) states.

Fig. 7. (a) Fabricated sensor from top(left) and bottom(right) view, (b) Sensing deployment.

that result in $Q_0 = \frac{f_0}{\Delta f}$. Another interesting observation of the sensor performance can be made by examining the Smith chart shown in Fig. 5. The characteristics are obtained from port 1 of the simulator for various values of negative resistance. It is clear that the Smith chart represents better matching for the curves located close to the central point (1, 0). This is achieved with partial loss compensation for the case $R = -132.5$ Ω. However, even though the transmission loss is fully compensated, the total loaded quality factor is still not satisfactory. It needs further improvement, which entails higher negative resistance values resulting in higher values of Q. However, the reflection coefficient is also high, resulting in the Smith chart circle to move away from the central point. This high reflection, in some cases, may result in damage to the measurement devices. Therefore an attenuator is needed to quench the reflections in both pathways to the vector network analyzer. In a commercial implementation, this could be avoided with the inclusion of line couplers before both ports 1 and 2 of Fig. 3. It should also be noted that the resonance profiles in Fig. 5 are shown with a different circulation of the Smith circle that corresponds to either a pole (left resonance) or a zero (right resonance).

The non-contact feature of the sensor enables it to interrogate the adjacent materials. The level of this interaction affects the dynamic range of the material location with respect to the sensor. This range is limited in the passive resonator design, mainly due to the lost power as a path loss when the input power is transmitted from the resonator to the material. In the proposed design, this problem is ultimately addressed using a custom active circuitry. It enables a wider range of operation, especially when the material under test is distant due to poor accessibility. Use of loss-compensation techniques provides higher sensitivity to materials when they are located at a distance with respect to the sensor. Illustration of the electric field magnitude in Fig. 6 shows different ranges of propagation on the surface (Fig. 6(a)), and in the surrounding space (Fig. 6(b)), through a vertical cross section. It is evident that the slots are highly heated in the diagram, indicating a good potential for interaction with external materials. Moreover, the
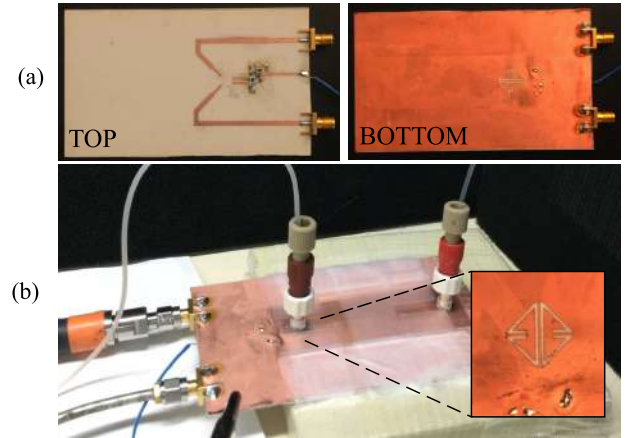
deeper extension of the electric field into the free space proves the sensor's capability in dealing with lossy environment and materials.

III. MEASUREMENT AND DISCUSSION

The proposed sensor is fabricated on Rogers RO3003 substrate as illustrated in Fig. 7(a) that shows the top and bottom sections separately. The fabrication process includes printing patterns on both the top and bottom sides of the substrate using a laser printer and etching unmasked sections with ammonium per-sulphate in water solution. In this specific design, special care must be taken to consider the alignment of the two designs on both sides of the substrate to establish a correct coupling between the resonators and transmission lines of the active circuit. This in-house etching method is followed by soldering the surface mount devices on the substrate. In the following step, the performance of the fabricated sensor is verified in terms of working with external liquids. A μfluidic channel, purchased from ChipShop [6], is taped on the sensor with an embedded channel which is $150\mu m$ thick and 2.5 mm wide as shown in Fig. 7(b). A small 175 μm lid separates the channel from the surface of the sensor. PTFE tubing and fitting are used to carry the injected fluid into and out of the μfluidic channel. Input port of the sensor is connected to an attenuator to remove the possible high reflections of the loss-compensated sensor back to the network analyzer. All connections are through phase-stabilized cables to preserve the sensitive phase information. The measurement results are controlled with various bias points through V_c, which essentially powers the amplifier on at different states.

A. Sensor Calibration with Chemicals and Glucose

In this section, the sensor response is calibrated with respect to the simulation results obtained by standard permittivity values of the materials with the sensor in active mode. The loss compensation of the sensor is achieved with a bias voltage of $V_C = 1.8$ V, wherein the left resonance (see Fig. 4(a)) is dominantly compensated. Various common chemicals including IPA, ethanol, methanol, and water are injected into the
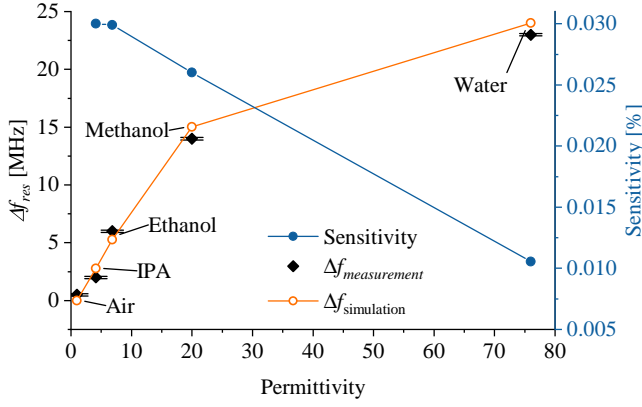
Fig. 8. Resonance frequency difference compared to air in simulation and measurement and corresponding sensitivity for various common chemicals inside μfluidic channel.

TABLE I
DIELECTRIC PROPERTIES OF COMMON CHEMICALS.

Chemical	IPA	Ethanol	Methanol	Water
Permitivity ε_r	4.13	6.8	20	76
Loss tangent $\tan(\delta)$	0.57	0.8	0.68	0.14

channel made of polymethyl methacrylate (PMMA) with 150 μm thickness that is separated from the sensor surface with a 175 μm lid. The measured resonance frequency shift from air is shown in Fig. 8 for all samples. The sensitivity of the design $S = [f_0 - f_{res}]/[f_0(\varepsilon_r - 1)]$, where f_{res} is the the resonance frequency because of the material with ε_r and f_0 is that of the bare resonance. In parallel, simulation of the proposed design in Ansys HFSS is conducted on material permittivity values at 3.5 GHz as given in Table I. The simulation results, shown in Fig. 8, incorporate active circuit symbolized with the equivalent negative resistance of $R = -180 \ \Omega$ and the phase of $126°$. The resonance frequency shifts increases as a result of higher permittivity values, which demonstrates high agreement between simulation and measurement relative results. Inaccuracy of the sensor response can be evaluated from the percentage difference between the simulated and measured responses, which is capped at $0.02 \ \%$ on average. The benefit of using a coupling region between two resonators is that the corresponding sensitivity drop at higher permittivity values is not drastic. This feature enables the proposed sensor to present a decent sensitivity up to $0.03 \ \%$ as shown in Fig. 8 considering a tiny sample volume of $4.5 \ \mu L$ inside a μfluidic channel. Also, the dynamic range of the sensor encompasses common permittivity range from 1 up to 80 that corresponds to $\Delta f = 24 \ MHz$ frequency shift. In addition, the dynamic range of the sensor can be extended by optimizing this coupling, compared with a microwave sensor utilizing only one resonator. In the next section, the interaction of the proposed sensor with a lossy medium is discussed in greater detail.

In addition to common chemicals, the proposed sensor response is evaluated for various glucose concentrations in the range of 50 up to 400 mg/dL with 50 mg/dL increments. These
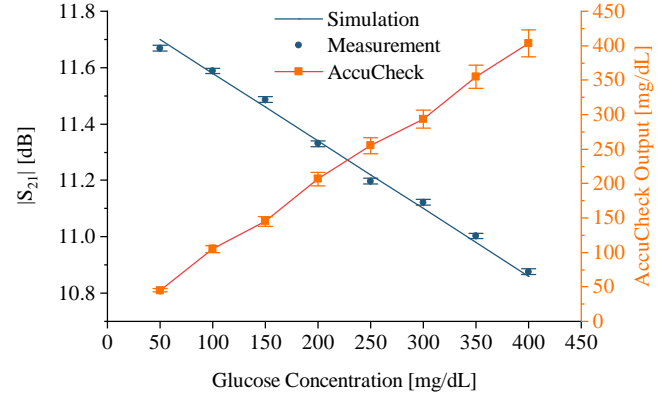

Fig. 9. Amplitude shift in simulation/measurement of the proposed sensor with corresponding AccuCheck response with respect to different concentrations of glucose in DI water [50: 50: 400] mg/dL.
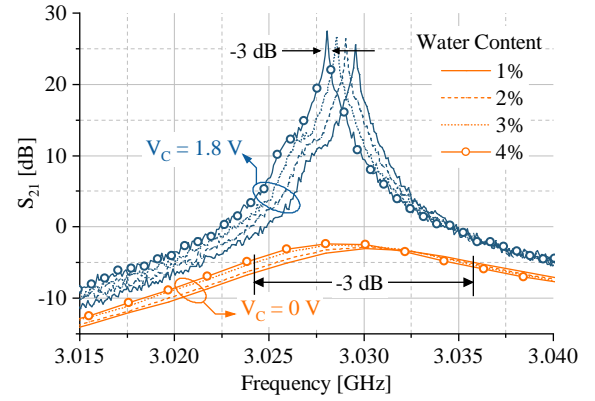

Fig. 10. Measured sensor transmission response in passive and active mode of operation.

samples are individually prepared with dissolving glucose powder in DI water as a baseline for sensor calibration. The corresponding dielectric properties of glucose solutions are imported into simulation model and the transmission amplitude $|S_{21}|$ is analyzed as shown in Fig. 9. Measurements are replicated for 3 times to obtain repeatable results with inaccuracies of $< 10 \ mdB$. The accuracy of AccuCheck glucometer is also verified on the prepared samples with the results shown in Fig. 9 that represent $< 10 \ \%$ inaccuracy in the glucose level. This measurement depicts the high accuracy of the proposed sensor along with decent performance from the commercial gauge.

B. Water in Ethanol Sensing

To evaluate the ability of the proposed sensor to deal with minute changes in the environment (closer to the limit of detection), various concentrations of water in ethanol were prepared and tested with the sensor. A μfluidic channel was mounted on the sensor to carry the solution, as shown in Fig. 8(b). The binary solution is created using two syringe pumps containing water and ethanol. The pumps are set to flow at different speeds so that the water in the ethanol solution's concentration varies within the range of 1% up to 4%. This
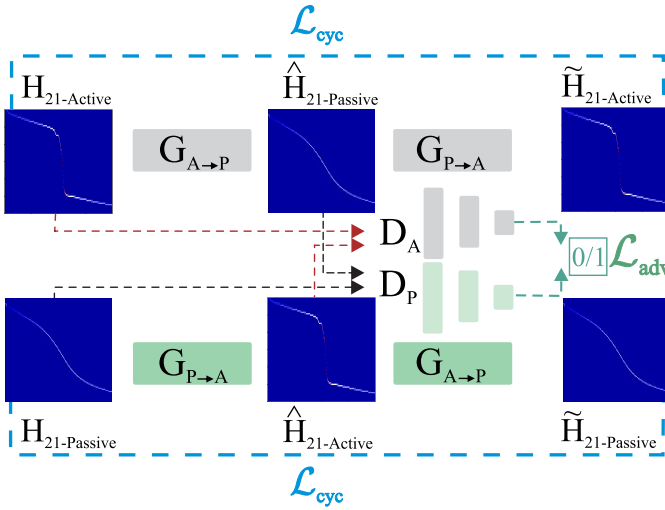
Fig. 11. Structure of CycleGAN. $G_{A \rightarrow P}$ and $G_{P \rightarrow A}$ denote active-to-passive and passive-to-active generators. Discriminators of passive and active domain are shown as D_A and D_P, respectively. Cycle consistency loss is represented as $\mathcal{L}_{cyc}$.

Fig. 12. Developing heat map diagrams from S-parameter recordings. (a) Magnitude and phase of S_{21}, (b) Generated heat map diagram.

variation in the amount of water is smaller than the resolvable range in the passive mode of operation as shown in Fig. 10(a). A high-fidelity sensing response in bandpass filters, such as the current work, considers a variation that causes the shifted resonance profiles not to overlap within a 3-dB bandwidth region.

The passive mode of operation leads to a confusing response with the majority of the transmission profiles overlapping one another. This makes it very difficult to discern the differences between the individual profiles. To ensure a more robust performance of the sensor, its loss-compensated response is also measured with the same solutions of water in ethanol. As shown in Fig. 10(b), the high loaded quality factor of the active sensor results in a higher fidelity of its response. This remarkably enhances the applicability of sensor for detecting smaller quantities of materials.

The high fidelity of the sensor response is due to the active circuitry and the delicate phase compensation. However, this approach also requires high power consumption at higher frequencies and it hits high frequency-related technology bottlenecks for circuit design. In addition, scalability of the active sensor for use in other platforms including microwave, ultrasound, and optical, is burdensome. To cope with these limitations associated with the use of active circuit, in this work, we introduce a novel technique that expands the applicability of the sensor in passive mode using machine learning. The use of CycleGAN transformation enhances the response of a regular sensor, enabling its use for sensitive measurements and high-end applications. The principle of operation of CycleGAN and its application to the measured sensing data are described in the next section.

IV. ARCHITECTURE OF CYCLEGAN MODEL

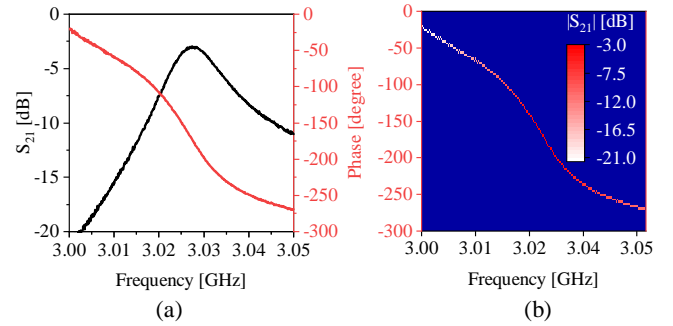Mapping between an input image and an output image is a subset of image processing problems conventionally performed using a collection of paired images that share some common features. Recently, transfer of images from one domain into another without much feature overlap has become an interesting topic in machine learning [42], [53], [54]. However, in many situations, there are not enough paired images to uniquely define the mapping. In such cases, the learning process can be supervised on the level of the whole training by the CycleGAN algorithm.

In this work, CycleGAN is used to overcome the limitations of passive sensors outlined in the previous section. Drawing on the definitions common in image processing, the input/output images refer to the representations of the sensor response in the passive/active modes. CycleGAN algorithm is used to learn the relationship between the responses in the two modes. It captures the characteristics of active responses and applies them to passive responses, all without the need of a paired training set.

Conventionally, the low-Q factor of the passive resonance profile is the main attribute preventing high-resolution sensing. The proposed method transfers the low-Q profiles into the equivalent high-Q profiles to facilitate sensing with high-resolution. In this algorithm (see Fig. 11), a mapping $G_{P \mapsto A}$ is trained to transform an image p from the passive domain P into another image $\hat{a}$ in the active domain A. The new image $\hat{a} = G_{P \mapsto A}(p)$ is expected to be indistinguishable from other images in the active domain $a \in A$. The model includes two discriminators D_A and D_P such that D_P distinguishes between the input image p and the translated image $\hat{p} = G_{A \mapsto P}(a)$, while D_A discriminates between a and the translated images $\hat{a} = G_{P \mapsto A}(p)$. In order to use this scheme on the sensor dataset, the recorded transmission profiles are converted into images as follows. The main contributing factor in the measurement of a two-port system is the transmission parameter (S_{21}), which is a complex-valued vector. A simple plot of only amplitude of S_{21} or its phase over frequency creates line graphs. However, one can combine these two graphs as shown in Fig. 12 into a single plot by embedding the values of magnitude as RGB colors in the plot of phase vs. frequency. The generated heat map, called H_{21} hereafter, is then considered an input image. This conversion results in 512 bins for each frequency and phase. The pixels can accept a combination of three colors of red (R), green (G), and blue (B). Therefore, a single measurement is reshaped into an image with a data volume of size $512 \times 512 \times 3$.
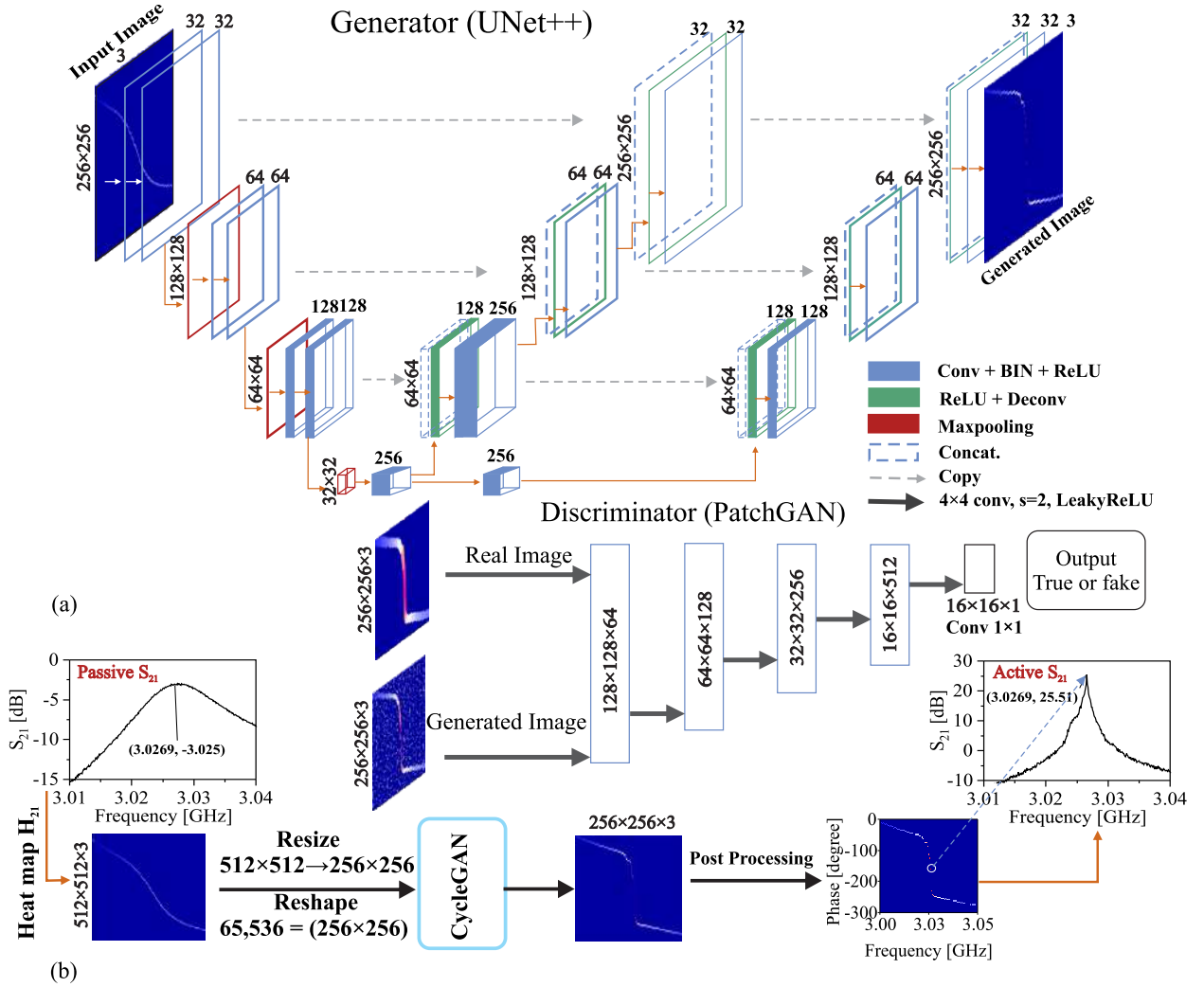
Fig. 13. (a) The Architecture of generator and discriminator, (b) A workflow of data preparation to generate the active S_{21} profile from passive.

The proposed method uses CycleGAN to translate the passive domain P into the active domain A, where the distribution of both are forced to be identical using adversarial loss [55]. Since this transformation model might result in many-to-one mappings, consistency of the transformation cycle must be preserved to avoid this ambiguity. To achieve this, the translator $G_{P \mapsto A}$ is accompanied with its inverse $G_{A \mapsto P}$ that converts the active domain into the passive one. This is implemented by using the output of one generator as the input of the other generator and combining the two mappings with a cycle consistency loss [48] that reinforces $G_{A \mapsto P}(G_{P \mapsto A}(p)) \approx p$ and $G_{P \mapsto A}(G_{A \mapsto P}(a)) \approx a$. Therefore, the objective function of CycleGAN is composed of adversarial loss as well as cycle consistency loss. The adversarial loss represents the difference between the real and estimated images, such that in generator G and discriminator D, the cost function is defined as follows:

$$\mathcal{L}(G_{A \mapsto P}, D_P) = \min_{\theta_g} \max_{\theta_d} \{ \mathbb{E}_{\mathbb{P}}[\log D_P(h_{21P})]$$
$$+ \mathbb{E}_{\mathbb{A}}[\log(1 - D_P(G_{A \mapsto P}(h_{21A})))] \}, \quad (12)$$

where p and a are the unpaired training datasets, and $\mathbb{E}_P$

and $\mathbb{E}_A$ are the expectations in the output and input images. The discriminator D_A and generator $G_{(P \mapsto A)}$ are trained synchronously within a $\min \max$ game style with weights θ_g and θ_d.

Input and output images of P and A are trained simultaneously, even though they are different representations. Thus, cycle loss is used to encourage the consistency between forward and backward training. Then, a secondary consistency loss is defined as follows:

$$\mathcal{L}_{\text{cyc}}(G_{A \to P}, G_{P \to A}) = \| G_{P \to A}(G_{A \to P})(h_{21A}) - h_{21A} \|_1$$
$$+ \| G_{A \to P}(G_{P \to A})(h_{21P}) - h_{21P} \|_1, \quad (13)$$

where $\| \cdot \|$ is L_1 loss and h_{21} denotes the heat map of the measured transmission response. The overall loss function of CycleGAN combines the two aforementioned losses as follows:

$$\mathcal{L}(G_{A \to P}, G_{P \to A}, D_A, D_P) = \mathcal{L}(G_{A \to P}, D_P)$$
$$+ \mathcal{L}(G_{P \to A}, D_A) + \lambda \mathcal{L}_{\text{cyc}}(G_{A \to P}, G_{P \to A}) \quad (14)$$

Algorithm 1 Minibatch stochastic gradient descent training of CycleGAN

Input: Minibatch H_{21} Heat Maps $\rightarrow$ $H_{21Active} \in$ A (source domain) and $H_{21Passive} \in$ P (target domain)
Output: Update network weights $\theta_{g(A \rightarrow P)}$, $\theta_{g(P \rightarrow A)}$, $\theta_{d(A)}$, $\theta_{d(P)}$
Initializing discriminator and generator weights.

1: **for** number of training iterations **do**
2:     $(\hat{H}_{21Passive},\ \tilde{H}_{21Active}) \leftarrow (G_{(A \rightarrow P)}H_{21Active}),\ (G_{(P \rightarrow A)}\hat{H}_{21Passive})$
3:     $(\hat{H}_{21Active},\ \tilde{H}_{21Passive}) \leftarrow (G_{(P \rightarrow A)}H_{21Passive}),\ (G_{(A \rightarrow P)}\hat{H}_{21Active})$
4:     $\mathcal{L}_{D(A),(P)} = \frac{1}{m}\sum_{i=1}^{m}[logD(H_{21-(A),(P)}^{i}) + log(1 - D(H_{21-(A),(P)}^{i}))]$ {Calculate D_P, D_A Loss}
5:     $\theta_{d(A),(P)} \leftarrow \theta_{d(A),(P)} - \eta\nabla_{d(A),(P)}\mathcal{L}_{cyc}$ {Update discriminator parameters}
6:     $\mathcal{L}_{cyc} = \lambda_1 \left\|\tilde{H}_{21Active} - H_{21passive}\right\|_1 + \lambda_2 \left\|\tilde{H}_{21Passive} - H_{21Active}\right\|_1$
7:     $\mathcal{L}_{G(A \rightarrow P)} \leftarrow \frac{1}{m}\sum_{i=1}^{m}(1 - logD_p(\hat{H}_{21passive}^{i})) + \mathcal{L}_{cyc}$ {Calculate $G_{(A \rightarrow P)}$ Loss}
8:     $\theta_{g(A \rightarrow P)} \leftarrow \theta_{g(A \rightarrow P)} - \eta\nabla_{\theta_{g(A \rightarrow P)}}\mathcal{L}_{G(A \rightarrow P)}$ {Update $G_{(A \rightarrow P)}$ Parameters}
9:     $\mathcal{L}_{G(P \rightarrow A)} \leftarrow \frac{1}{m}\sum_{i=1}^{m}(1 - logD_A(\hat{H}_{21active}^{i})) + \mathcal{L}_{cyc}$ {Calculate $G_{(P \rightarrow A)}$ Loss}
10:    $\theta_{g(P \rightarrow A)} \leftarrow \theta_{g(P \rightarrow A)} - \eta\nabla_{\theta_{g(P \rightarrow A)}}\mathcal{L}_{G(P \rightarrow A)}$ {Update $G_{(P \rightarrow A)}$ Parameters}
11: **end for**

---

where λ is a hyperparameter to balance the loss terms, meaning that the consistency loss is λ times more important than the adversarial loss. In this case, the generators are trained to produce fake images as close to real ones as possible; and the discriminators are employed to distinguish more appropriately between real and fake images. The training stops when the discriminators reach close to 0.5 probability estimate for fake image discrimination.

A. Implementation

The proposed CycleGAN network consists of a generator and a discriminator in the source domain and another identical pair in the target domain. The passive-to-active generator network shares its characteristics with the active-to-passive network; similarly, the active discriminator D_A resembles to the passive one D_P. In the next sections, the generator and discriminator of the design are elaborated.

1) Generator Structure: The generator (see Fig. 13) is based on U-net [56] architecture; further inspired by U-net++ [57], the encoder and decoder are linked through a middle layer. This helps smoother integration of shallow and deep features. Normally-distributed weights in each layer allow deeper model connections to be used for complex scenarios. The structure of the generator can be summarized as follows. Let us consider CK as a 3×3 Convolution-BatchInstanceNormReLU layer (C) with K filters and stride 1. M denotes Maxpooling layer. DK denotes a 2×2 TransposedConvolutionalLayer-BatchInstanceNormReLU layer with K filters and stride 2, and 6 Concatenate blocks denoted as Concat.
C32, C32, M, C64, C64, M, C128, C128, M, C256, C256, D128, Concat., C128, D128, Concat., C128, D64, Concat., C64, D64, Concat., C64, D32, C32, D32, Concat., C32, C3.

2) Discriminator Structure: In the discriminator, real- or fake patches of the images are discriminated using Markovian discriminator (PatchGAN) [58]. Compared with regular full-sized image discriminators, this method uses less computational resources and is compatible with various image sizes. In addition, the use of least squares loss increases the robustness

TABLE II
MSE, PSNR AND SSIM COMPARISON OF DIFFERENT ALGORITHMS.
REFERENCE: ACTIVE SENSOR RESPONSE.

Methods	MSE	PSNR	SSIM
pix2pix	0.02	17.7194	0.4871
Conventional CycleGAN	0.0049	23.0437	0.7865
This work	0.00146	28.34	0.9167

of its operation. Layers of the discriminator include filters with sizes of 64, 128, 256, and 512. The first four layers have a kernel size of 4×4 with LeakyRelu activation function (to introduce a small positive gradient when a neuron is not active), followed by the last layer with a sigmoid function. The discriminator architecture is:
C64, C128, C256, C512.

3) Training: The heat map images (512×512) are resized to (256×256) to be computationally efficient in the training process. Reshaped images are fed to the conventional UNet++ except for the batch normalization layer that is simply replaced with batch-instance normalization (BIN) [59] to normalize the styles adaptively to the task and selectively to individual feature maps. Using BIN, the amount of style information that needs to be propagated through each channel of features is controllable by a learnable gating parameter. To make the model more general and benefit from both batch normalization (BN) in multiclass classification and instance normalization (IN) in style transfer networks, IN and BN are substituted by BIN. The networks are trained using stochastic gradient descent (SGD) with a batch size of 32, momentum of 0.9, weight decay of 0.0001, and initial learning rate of 0.1. The network is trained for 150 epochs, where the learning rate is divided by 10 at epochs 50 and 100. The entire procedure is formally presented in Algorithm 1.

B. High-resolution Sensor Response Using CycleGAN

In this section, the measured sensor response to water in ethanol solution is reevaluated with the CycleGAN network applied to the measured heat maps. Four solutions with 1%, 2%, 3%, and 4% water in ethanol are measured using the
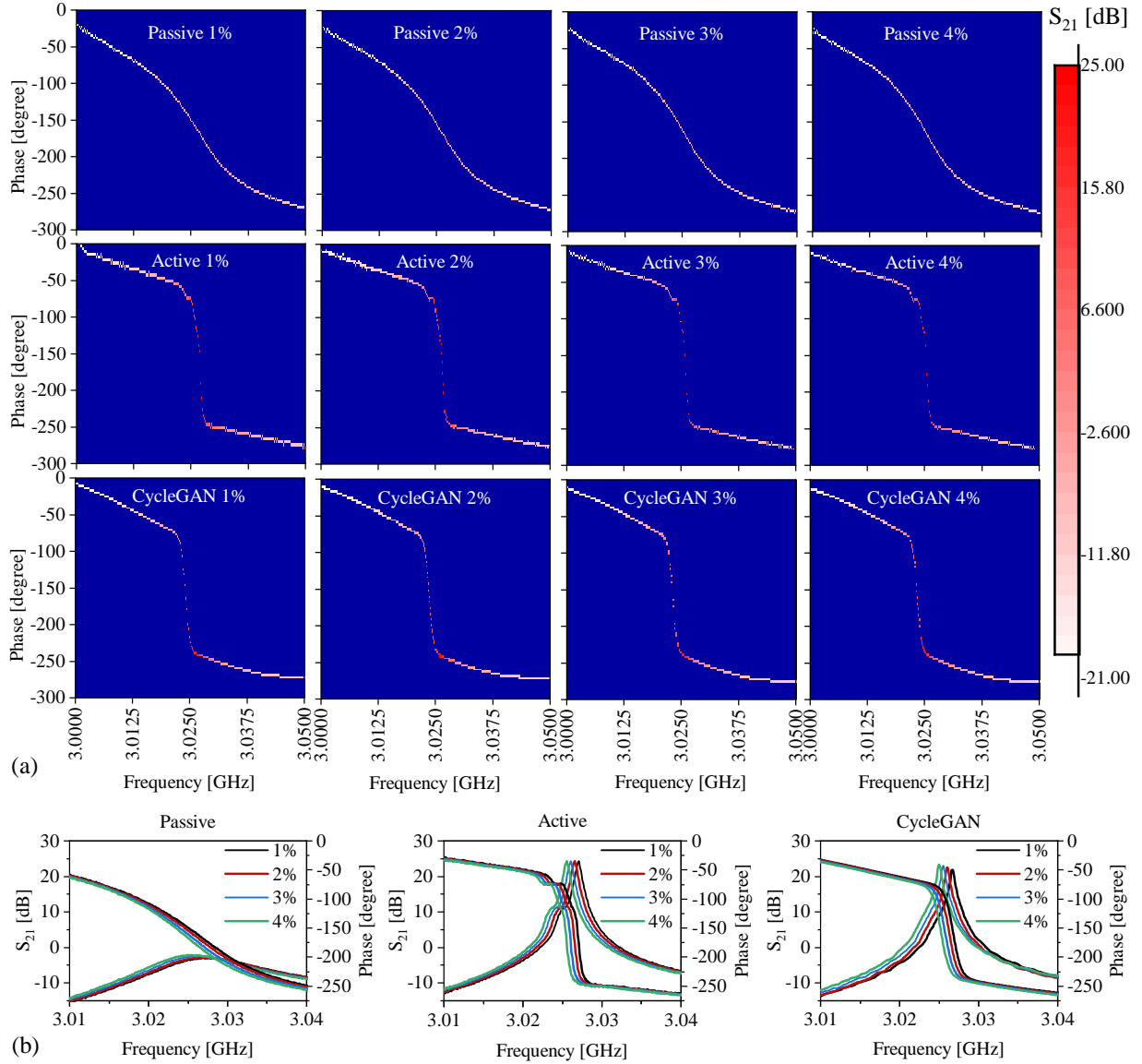
Fig. 14. (a) Equivalent heat maps for one sample of 1%, 2%, 3%, and 4% water in ethanol using the sensor in passive mode (top row), active mode (middle row), and passive mode aided with CycleGAN (bottom row), (b) Measured sensor response for one sample of 1%, 2%, 3%, and 4% water in ethanol passive mode (left), active mode(middle), and CycleGAN-boosted passive mode (right)

proposed sensor in both passive and active operating regime. The prepared solutions are passed through the μfluidic channel and the sensor responses are recorded using LabView with 5-second time resolution. The solution is passed through the channel to obtain a total of 200 sample measurements per recording before the syringe is emptied out. This process is repeated five times to acquire enough data for training purposes. Each recorded sample is then converted into its equivalent heat map (H_{21}) which combines the information on the amplitude and phase of resonance. Plots in the top and middle rows of Fig. 14(a) show the heat maps obtained using the passive and active mode, respectively. Corresponding profiles obtained using CycleGAN trained for 150 epochs are shown in the bottom row of the figure. The output of this transformation is a new heat map trained to be similar to the heat map obtained from the active sensor data.

A magnitude-and-phase representation of the four measured solutions is shown in Fig. 14(b), including the passive -domain measurements as well as the active-domain representation used as the target for CycleGAN training. The outputs obtained by mapping the passive-domain representations through the trained network are also included. The general shape of the high-resolution profiles clearly visible in the output response of CycleGAN, although there are some nuances in the absolute values of the S_{21} magnitude at the resonance frequency. The high-resolution response of the sensor using CycleGAN has a loaded quality factor of $Q_{\text{CycleGAN}} \approx 5040$, which exhibits resolution more than 20 times higher than that of passive domain $Q_{\text{Passive}} \approx 230$. The frequency dependent resolution of the sensor in active mode reduces down to $\approx 100\ kHz$ from $\approx 1\ MHz$ of passive case. The similarity between CycleGAN-boosted response and the active sensor response is
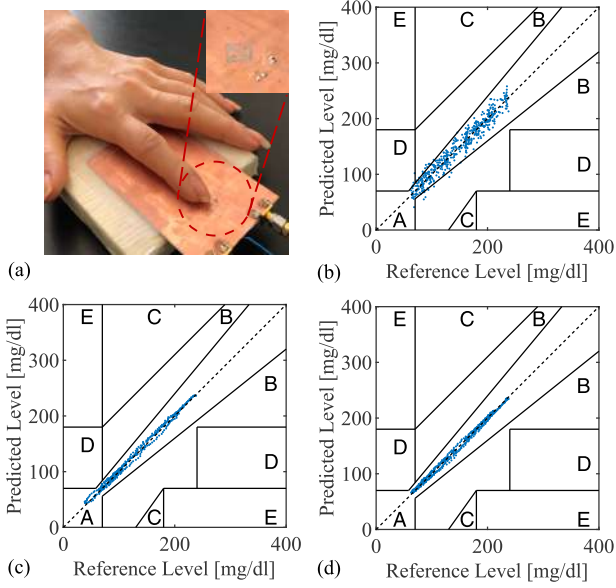
Fig. 15. (a) Fingertip measurement Setup, Clarke error grid analysis for (b) Passive, (c) Active , (d) CycleGAN-boosted passive states of the sensor response.
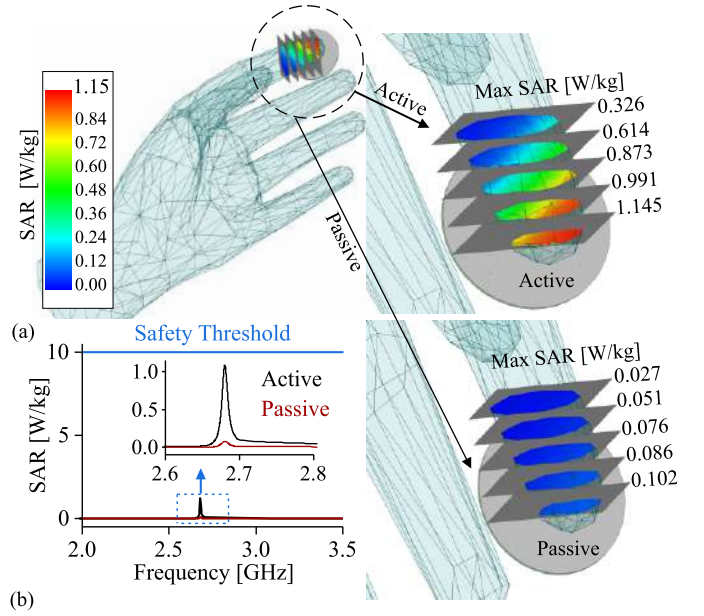

Fig. 16. (a) Simulated SAR on hand when finger is placed on the sensor, (b) Simulated SAR across frequency for active and passive states of the sensor.

evaluated in Table II in terms of several common metrics [60], [61]. The approach introduced in this contribution is compared to pix2pix cGAN [62] and to conventional CycleGAN [48]. The proposed network outperforms both algorithms with high SSIM of 0.9167 and low MSE of 0.00146. This is mainly due to replacing the ResNet (9 residual block for 256×256 generator) of conventional CycleGAN [48] with UNet++ [57] and also substituting instance normalization with batch-instance normalization [59]. BIN allows replacing Adam optimizer with SGD, which results in better performance of the network.

C. Glucose Sensing

In another experiment to evaluate the proposed approach, the CycleGAN-enhanced sensor is employed in an noninvasive glucose sensing application [1]. The glucose content increases in the blood as a result of food intake. It gradually drops over time while being absorbed by the cells. This fluctuation in the blood glucose level becomes apparent in the interstitial fluid under the skin with minutes of delay. This leaves a reliable trace of the actual glucose level deep inside veins. Non-contact sensing has already shown robustness in glucose sensing using active regime with high sensitivity and reasonable fidelity. This has been achieved using sophisticated active circuitry, which requires constant powering for continuous operation. An alternative solution can be developed using the approach proposed in this article: the passive sensor response can be boosted using CycleGAN. This alternative preserves the high-Q performance normally offered by the active circuit design, while using zero-power sensors.

The performance of CycleGAN-boosted glucose sensor was evaluated using the following experiment. A participant, not suffering from diabetes, underwent continuous monitoring of their glucose level. The sensing was noninvasive, implemented

by placing the subject's index finger on the sensitive region of the sensor as shown in Fig. 15(a). Since the glucose content of the interstitial fluid changes the dielectric constant of the skin, the participant's right finger was placed in the close proximity of the sensor surface. While the participant was asked to minimize their movement during the experiment, the transmission profile of the sensor was measured continuously. During this process, 500 data points were recorded with 20-second resolution and the participant was fed at different times to control the glucose level.

An Accu-Check commercial glucometer was used to measure the blood glucose on the left hand finger of the participant every 5-minutes. The collected measurements serve as a reference for calibrating the sensor response. Using this technique, the resonance frequency and amplitude are correlated to the change in blood glucose level. Passive sensor response, due to its low-to-moderate loaded quality factor, is more prone to environmental amplitude noise. Considering this concept, measurements of the sensor response in both passive and active regime (performed separately) are analyzed to extract the resonance frequency. For the passive resonance profile, its heat map is generated and fed into CycleGAN to obtain high-loaded quality factor equivalent heat maps. Subsequently, the resonance profile S_{21} is extracted from the corresponding heat maps. The resonance frequency is the most importance feature of the CycleGAN-generated heat map from CycleGAN as it must exactly correspond to the original frequency of operation. To ensure this correspondence, the cycle consistency loss is used to preserve the resonance frequency.

The accuracy of the proposed sensor in detecting glucose levels is evaluated using Clarke error grid analysis (EGA) [63]. The results of this analysis, performed on 500 recordings of the interstitial glucose level, are illustrated in Fig. 15. The horizontal axis represents the reference glucose level obtained

from the commercial glucometer, while the vertical axis shows the level inferred using the proposed approach.

For the passive sensor response (see Fig. 15(b)), 96.2% of paired sensor reference values fall into region A, which holds 20% of the reference values. Region B, which has next 20% of reference values in a form acceptable for treatment, contains 3.19% of pairs. In this evaluation, regions C and E do not contain any paired data. However, 0.59% of the data pairs fall in region D, which indicates potentially dangerous failure to detect low or high levels of glucose. The apparently scattered data points of the passive sensor Clarke EGA confirm that the low-resolution output can lead to unreliable detection of resonance frequency. This observation is further supported by relatively large values of root of mean squared error (RMSE) of 11.31, mean relative absolute deviation (mRAD) of 7.08, and mean absolute error (MAE) of 9.09.

For comparison, the same sensor was used in active mode of operation in the following day. The experimental setting including the measurement time, duration, fasting mode, food intake pattern, and the participant remained identical to the passive mode measurement conditions to avoid endogenous/exogenous masking effects. Since this measurement were conducted in a different session, the results do not correspond to the passive sensor measurements directly. However, they can be used to compare the general precision between the two sensor state operating modes. With loss compensation in the circuit, the prediction of glucose level became more precise with much less noise infused into the sensor response. The resonance frequency of each profile was extracted in correspondence to each reference glucose level as shown in Fig. 15(b) and Clarke EGA was also applied to this data. It is shown that the spread of the predicted values is confined within a limited area, closer to the diagonal line. The compositional analysis of these measurement shows that all 100% datapoints are located in the zone A. The errors measures also attain much lower values of RMSE = 3.53, mRAD = 2.22, and MAE = 2.85.

Considering the improvements obtained using the active sensor data, the result of the passive sensor were also analyzed after CycleGAN transformation. As shown in Fig. 15(c), the spread of datapoints of Clarke EGA is significantly reduced compared to that of datapoints obtained using passive sensor directly and all datapoints fall into zone A. The values of error metrics are also in line with active sensor response, i.e. RMSE = 4.013, mRAD = 3.14, and MAE = 3.17. The considerable improvement between the passive sensor response and the CycleGAN-boosted response confirms the high potential of the proposed technique as a general method for improving sensing performance. This approach is not limited to microwave sensors but could be extended to various other applications.

The electromagnetic wave absorption of the proposed sensor when being applied to human skin is also simulated in full-wave simulator HFSS. While the skin is being monitored continuously, the specific absorption ratio (SAR) is computed at the frequency of operation and averaged over 10g of tissue that is considered with the average human hand model as shown in Fig. 16(a). Maximum SAR values at different cross-sections of the finger tip is shown in both passive (R=-0.1

kΩ) and active states (R=-0.2 kΩ) of the sensor according to Fig. 16. The maximum SAR values across all hand volume over a wide range of frequencies is also shown in Fig. 16(b), which depicts a fair margin for SAR values (max(SAR)<1 W/kg) compared with the safety threshold of 10 W/kg. This reassures safe range of applications for clinical trials and wearable applications.

V. CONCLUSION

In this work, we introduce a CycleGAN-boosting algorithm as a learnable technique to improve the sensing performance of low-quality resonance-based sensor response. In particular, an ultra-high sensitive microwave sensor that leverages a coupled CSRR design is used as a core of a loss-compensated active sensor to work at ≈ 3.5 GHz. The mutual coupling between the resonators provides a region with strongly enhanced sensitivity. The sensor performance in the loss-compensated mode is significantly improved, with ≈ 10-fold increase of the loaded quality factor compared to the passive mode response. However, to avoid the complexity of circuit design and the need for constant powering, a novel method is introduced that involves a learning network called CycleGAN. It maps the measured passive mode S_{21} response of the sensor to an equivalent active mode response while increasing the S_{21} loaded quality factor. It is shown that while low concentration of water in the mixture of water in ethanol results in intermingled transmission profiles, applying CycleGAN on the passive mode sensor response not only improves their loaded quality factor by an order of magnitude, but also helps differentiate them with higher resolution. Following the same procedure for noninvasive glucose detection, the CycleGAN-boosted sensor response results in very low measurement errors, as confirmed by Clarke error grid analysis. This technique is potentially applicable to a wide range of applications, where high-end sensing can be conducted with low-profile sensors amended with machine learning methods.

REFERENCES

[1] M. Abdolrazzaghi, N. Katchinskiy, A. Elezzabi, P. E. Light, and M. Daneshmand, "Noninvasive glucose sensing in aqueous solutions using an active split-ring resonator," *IEEE Sensors Journal*, 2021.

[2] M. Baghelani, Z. Abbasi, M. Daneshmand, and P. E. Light, "Non-invasive continuous-time glucose monitoring system using a chipless printable sensor based on split ring microwave resonators," *Scientific Reports*, vol. 10, no. 1, pp. 1–15, 2020.

[3] T. Athauda, P. C. Banerjee, and N. C. Karmakar, "Microwave characterization of chitosan hydrogel and its use as a wireless ph sensor in smart packaging applications," *IEEE Sensors Journal*, vol. 20, no. 16, pp. 8990–8996, 2020.

[4] M. Abdolrazzaghi, M. Daneshmand, and A. K. Iyer, "Strongly enhanced sensitivity in planar microwave sensors based on metamaterial coupling," *IEEE Transactions on Microwave Theory and Techniques*, vol. 66, no. 4, pp. 1843–1855, 2018.

[5] N. Kazemi, M. Abdolrazzaghi, P. Musilek, and M. Daneshmand, "A temperature-compensated high-resolution microwave sensor using artificial neural network," *IEEE Microwave and Wireless Components Letters*, vol. 30, no. 9, pp. 919–922, 2020.

[6] E. L. Chuma, Y. Iano, G. Fontgalland, L. L. B. Roger, and H. Loschi, "Pcb-integrated non-destructive microwave sensor for liquid dielectric spectroscopy based on planar metamaterial resonator," *Sensors and Actuators A: Physical*, vol. 312, p. 112112, 2020.

[7] A. Hedayatipour, S. Aslanzadeh, S. H. Hesari, M. A. Haque, and N. McFarlane, "A wearable cmos impedance to frequency sensing system for non-invasive impedance measurements," *IEEE Transactions on Biomedical Circuits and Systems*, vol. 14, no. 5, pp. 1108–1121, 2020.

[8] R. A. Alahnomi, Z. Zakaria, Z. M. Yussof, A. A. Althuwayb, A. Alhegazi, H. Alsariera, and N. A. Rahman, "Review of recent microwave planar resonator-based sensors: Techniques of complex permittivity extraction, applications, open challenges and future research directions," *Sensors*, vol. 21, no. 7, p. 2267, 2021.

[9] E. L. Chuma, Y. Iano, G. Fontgalland, and L. L. B. Roger, "Microwave sensor for liquid dielectric characterization based on metamaterial complementary split ring resonator," *IEEE Sensors Journal*, vol. 18, no. 24, pp. 9978–9983, 2018.

[10] M. Saadat-Safa, V. Nayyeri, M. Khanjarian, M. Soleimani, and O. M. Ramahi, "A csrr-based sensor for full characterization of magneto-dielectric materials," *IEEE Transactions on Microwave Theory and Techniques*, vol. 67, no. 2, pp. 806–814, 2019.

[11] N. Kazemi, M. Abdolrazzaghi, and P. Musilek, "Comparative analysis of machine learning techniques for temperature compensation in microwave sensors," *IEEE Transactions on Microwave Theory and Techniques*, 2021.

[12] N. Kazemi, K. Schofield, and P. Musilek, "A high-resolution reflective microwave planar sensor for sensing of vanadium electrolyte," *Sensors*, vol. 21, no. 11, p. 3759, 2021.

[13] M. H. Zarifi, P. Shariaty, M. Abdolrazzaghi, Z. Hashisho, and M. Daneshmand, "Particle size characterization using a high resolution planar resonator sensor in a lossy medium," *Sensors and Actuators B: Chemical*, vol. 234, pp. 332–337, 2016.

[14] S. Mohammadi and M. H. Zarifi, "Differential microwave resonator sensor for real-time monitoring of volatile organic compounds," *IEEE Sensors Journal*, vol. 21, no. 5, pp. 6105–6114, 2020.

[15] K. K. Kazemi, S. Hu, O. Niksan, K. K. Adhikari, N. R. Tanguy, S. Li, M. Arjmand, and M. H. Zarifi, "Low-profile planar antenna sensor based on ti3c2tx mxene membrane for voc and humidity monitoring," *ADVANCED MATERIALS INTERFACES*, vol. 9, no. 13, 2022.

[16] O. Niksan, M. C. Jain, A. Shah, and M. H. Zarifi, "A nonintrusive flow rate sensor based on microwave split-ring resonators and thermal modulation," *IEEE Transactions on Microwave Theory and Techniques*, vol. 70, no. 3, pp. 1954–1963, 2022.

[17] A. Mason, M. Soprani, O. Korostynska, A. Amirthalingam, J. Cullen, M. Muradov, E. N. Carmona, G. Sberveglieri, V. Sberveglieri, and A. Al-Shamma'a, "Real-time microwave, dielectric, and optical sensing of lincomycin and tylosin antibiotics in water: Sensor fusion for environmental safety," *Journal of Sensors*, vol. 2018, 2018.

[18] I. Frau, S. Wylie, P. Byrne, P. Onnis, J. Cullen, A. Mason, and O. Korostynska, "Microwave sensors for in situ monitoring of trace metals in polluted water," *Sensors*, vol. 21, no. 9, p. 3147, 2021.

[19] C. Jang, J.-K. Park, H.-J. Lee, G.-H. Yun, and J.-G. Yook, "Non-invasive fluidic glucose detection based on dual microwave complementary split ring resonators with a switching circuit for environmental effect elimination," *IEEE Sensors Journal*, vol. 20, no. 15, pp. 8520–8527, 2020.

[20] M. Abdolrazzaghi, N. Kazemi, and M. Daneshmand, "Machine learning to immune microwave sensors from temperature impact," in *2020 IEEE International Symposium on Antennas and Propagation and North American Radio Science Meeting*. IEEE, 2020, pp. 843–844.

[21] M. Abdolrazzaghi and M. Daneshmand, "Multifunctional ultrahigh sensitive microwave planar sensor to monitor mechanical motion: Rotation, displacement, and stretch," *Sensors*, vol. 20, no. 4, p. 1184, 2020.

[22] M. Baghelani, Z. Abbasi, and M. Daneshmand, "High-dynamic-range chipless microwave resonator-based strain sensor," *IEEE Transactions on Instrumentation and Measurement*, vol. 70, pp. 1–7, 2021.

[23] M. Abdolrazzaghi, N. Kazemi, and M. Daneshmand, "Sensitive spectroscopy using dsrr array and linvill negative impedance," in *2019 IEEE MTT-S International Microwave Symposium (IMS)*, 2019, pp. 1080–1083.

[24] ——, "An siw oscillator for microfluidic lossy medium characterization," in *2020 IEEE/MTT-S International Microwave Symposium (IMS)*. IEEE, 2020, pp. 221–224.

[25] M. Abdolrazzaghi and M. Daneshmand, "Exploiting sensitivity enhancement in micro-wave planar sensors using intermodulation products with phase noise analysis," *IEEE Transactions on Circuits and Systems I: Regular Papers*, vol. 67, no. 12, pp. 4382–4395, 2020.

[26] Z. Abbasi, H. Niazi, M. Abdolrazzaghi, W. Chen, and M. Daneshmand, "Monitoring ph level using high-resolution microwave sensor for mitigation of stress corrosion cracking in steel pipelines," *IEEE Sensors Journal*, vol. 20, no. 13, pp. 7033–7043, 2020.

[27] A. M. Jones, J. F. Kelly, J. Tedeschi, and J. S. McCloy, "Design considerations for high-q bandpass microwave oscillator sensors based upon resonant amplification," *Applied Physics Letters*, vol. 104, no. 25, p. 253507, 2014.

[28] L.-C. Fan, W.-S. Zhao, H.-Y. Gan, L. He, Q. Liu, L. Dong, and G. Wang, "A high-q active substrate integrated waveguide based sensor for fully characterizing magneto-dielectric (md) materials," *Sensors and Actuators A: Physical*, vol. 301, p. 111778, 2020.

[29] M. Abdolrazzaghi, V. Nayyeri, and F. Martin, "Techniques to improve the performance of planar microwave sensors: A review and recent developments," *Sensors*, vol. 22, no. 18, p. 6946, 2022.

[30] T. Mosavirik, M. Hashemi, M. Soleimani, V. Nayyeri, and O. M. Ramahi, "Microwave permittivity characterization using power measurements and machine learning," in *2021 IEEE Indian Conference on Antennas and Propagation (InCAP)*. IEEE, 2021, pp. 618–620.

[31] ——, "Material characterization using power measurements: Miracle of machine learning," in *2021 51st European Microwave Conference (EuMC)*. IEEE, 2022, pp. 606–609.

[32] M. Abdolrazzaghi, R. Genov, and G. V. Eleftheriades, "Microwave planar sensor antenna for glucose sensing in aqueous solutions," in *2021 IEEE International Symposium on Antennas and Propagation and USNC-URSI Radio Science Meeting (APS/URSI)*. IEEE, 2021, pp. 127–128.

[33] L. Crossland, D. Askew, R. Ware, P. Cranstoun, P. Mitchell, A. Bryett, and C. Jackson, "Diabetic retinopathy screening and monitoring of early stage disease in australian general practice: tackling preventable blindness within a chronic care model," *Journal of diabetes research*, vol. 2016, 2016.

[34] K. Polat and S. Güneş, "An expert system approach based on principal component analysis and adaptive neuro-fuzzy inference system to diagnosis of diabetes disease," *Digital signal processing*, vol. 17, no. 4, pp. 702–710, 2007.

[35] N. Sattar, "Revisiting the links between glycaemia, diabetes and cardiovascular disease," *Diabetologia*, vol. 56, no. 4, pp. 686–695, 2013.

[36] A. S. d. M. Matheus, L. R. M. Tannus, R. A. Cobas, C. C. S. Palma, C. A. Negrato, and M. d. B. Gomes, "Impact of diabetes on cardiovascular disease: an update," *International journal of hypertension*, vol. 2013, 2013.

[37] A. J. Bandodkar, S. Imani, R. Nunez-Flores, R. Kumar, C. Wang, A. V. Mohan, J. Wang, and P. P. Mercier, "Re-usable electrochemical glucose sensors integrated into a smartphone platform," *Biosensors and Bioelectronics*, vol. 101, pp. 181–187, 2018.

[38] Y. Xue, A. S. Thalmayer, S. Zeising, G. Fischer, and M. Lübke, "Commercial and scientific solutions for blood glucose monitoring—a review," *Sensors*, vol. 22, no. 2, p. 425, 2022.

[39] J. Hanna, M. Bteich, Y. Tawk, A. H. Ramadan, B. Dia, F. A. Asadallah, A. Eid, R. Kanj, J. Costantine, and A. A. Eid, "Noninvasive, wearable, and tunable electromagnetic multisensing system for continuous glucose monitoring, mimicking vasculature anatomy," *Science Advances*, vol. 6, no. 24, p. eaba5320, 2020.

[40] P. Naseri, S. Pearson, Z. Wang, and S. V. Hum, "A combined machine-learning/optimization-based approach for inverse design of nonuniform bianisotropic metasurfaces," *arXiv preprint arXiv:2105.14133*, 2021.

[41] S. Qi and C. Sarris, "Deep neural networks for rapid simulation of planar microwave circuits based on their layouts," 2022.

[42] P. Naseri and S. V. Hum, "A generative machine learning-based approach for inverse design of multilayer metasurfaces," *IEEE Transactions on Antennas and Propagation*, vol. 69, no. 9, pp. 5725–5739, 2021.

[43] A. Seretis, T. Hashimoto, and C. D. Sarris, "A generative adversarial network approach for indoor propagation modeling with ray-tracing," in *2021 IEEE International Symposium on Antennas and Propagation and USNC-URSI Radio Science Meeting (APS/URSI)*. IEEE, 2021, pp. 657–658.

[44] N. Kazemi, N. Gholizadeh, and P. Musilek, "Selective microwave zeroth-order resonator sensor aided by machine learning," *Sensors*, vol. 22, no. 14, p. 5362, 2022.

[45] A. Seretis and C. D. Sarris, "An overview of machine learning techniques for radiowave propagation modeling," *IEEE Transactions on Antennas and Propagation*, 2021.

[46] T. Mosavirik, M. Hashemi, M. Soleimani, V. Nayyeri, and O. M. Ramahi, "Accuracy-improved and low-cost material characterization using power measurement and artificial neural network," *IEEE Transactions on Instrumentation and Measurement*, vol. 70, pp. 1–9, 2021.

[47] Y. Lu, Y.-W. Tai, and C.-K. Tang, "Attribute-guided face generation using conditional cyclegan," in *Proceedings of the European conference on computer vision (ECCV)*, 2018, pp. 282–297.

[48] J.-Y. Zhu, T. Park, P. Isola, and A. A. Efros, "Unpaired image-to-image translation using cycle-consistent adversarial networks," in *Proceedings of the IEEE international conference on computer vision*, 2017, pp. 2223–2232.

[49] L.-V. Herrera-Sepulveda, J.-L. Olvera-Cervantes, A. Corona-Chavez, and T. Kaur, "Sensor and methodology for determining dielectric constant using electrically coupled resonators," *IEEE Microwave and Wireless Components Letters*, vol. 29, no. 9, pp. 626–628, 2019.

[50] C. G. Juan, B. Potelon, C. Quendo, E. Bronchalo, and J. M. Sabater-Navarro, "Highly-sensitive glucose concentration sensor exploiting inter-resonators couplings," in *2019 49th European Microwave Conference (EuMC)*. IEEE, 2019, pp. 662–665.

[51] J. Aitken, "Swept-frequency microwave q-factor measurement," in *Proceedings of the Institution of Electrical Engineers*, vol. 123, no. 9. IET, 1976, pp. 855–862.

[52] J. Bray and L. Roy, "Measuring the unloaded, loaded, and external quality factors of one-and two-port resonators using scattering-parameter magnitudes at fractional power levels," *IEE Proceedings-Microwaves, Antennas and Propagation*, vol. 151, no. 4, pp. 345–350, 2004.

[53] V. Avkhimenia, T. Weis, and P. Musilek, "Generation of synthetic ampacity and electricity pool prices using generative adversarial networks," in *2021 IEEE Electrical Power and Energy Conference (EPEC)*, 2021, pp. 225–230.

[54] M. Sabuhi, M. Zhou, C.-P. Bezemer, and P. Musilek, "Applications of generative adversarial networks in anomaly detection: A systematic literature review," *IEEE Access*, vol. 9, pp. 161 003–161 029, 2021.

[55] I. Goodfellow, J. Pouget-Abadie, M. Mirza, B. Xu, D. Warde-Farley, S. Ozair, A. Courville, and Y. Bengio, "Generative adversarial nets," *Advances in neural information processing systems*, vol. 27, 2014.

[56] O. Ronneberger, P. Fischer, and T. Brox, "U-net: Convolutional networks for biomedical image segmentation," in *International Conference on Medical image computing and computer-assisted intervention*. Springer, 2015, pp. 234–241.

[57] Z. Zhou, M. M. R. Siddiquee, N. Tajbakhsh, and J. Liang, "Unet++: A nested u-net architecture for medical image segmentation," in *Deep learning in medical image analysis and multimodal learning for clinical decision support*. Springer, 2018, pp. 3–11.

[58] C. Li and M. Wand, "Precomputed real-time texture synthesis with markovian generative adversarial networks," *ArXiv*, vol. abs/1604.04382, 2016.

[59] H. Nam and H.-E. Kim, "Batch-instance normalization for adaptively style-invariant neural networks," *arXiv preprint arXiv:1805.07925*, 2018.

[60] A. Z Wang, H. C Bovik, R. Sheikh, and E. P. Simoncelli, "Image quality assessment: from error visibility to structural similarity," *IEEE transactions on image processing*, vol. 13, no. 4, pp. 600–612, 2004.

[61] D. R. I. M. Setiadi, "Psnr vs ssim: imperceptibility quality assessment for image steganography," *Multimedia Tools and Applications*, vol. 80, pp. 8423–8444, 2021.

[62] P. Isola, J.-Y. Zhu, T. Zhou, and A. A. Efros, "Image-to-image translation with conditional adversarial networks," 2018.

[63] I. M. Wentholt, J. B. Hoekstra, and J. H. DeVries, "A critical appraisal of the continuous glucose–error grid analysis," *Diabetes Care*, vol. 29, no. 8, pp. 1805–1811, 2006.

Nazli Kazemi received the B.Sc. degree from the Iran University of Science and Technology, Tehran, Iran, in 2018, and M.Sc. degree from the University of Alberta, Edmonton, AB, Canada, in 2020, all in Electrical and Computer Engineering. Her research interests include applications of machine learning in sensors, renewable energy systems, environmental sensing, monitoring, modeling, microwave active sensors, metamaterials, and biosensors. She continued pursuing graduate studies at the University of Alberta in 2020 as a PhD student in Electrical and Computer Engineering Department.

Petr Musilek (Senior Member, IEEE) received the Ing. degree (with great distinction) in Electrical Engineering and the Ph.D. degree in Cybernetics from the Military Academy in Brno, Czech Republic, in 1991 and 1995, respectively. In 1995, he was appointed the Head of the Computer Applications Group, Institute of Informatics, Military Medical Academy, Hradec Kralove, Czech Republic. From 1997 to 1999, he was a NATO Science Fellow at the Intelligent Systems Research Laboratory, University of Saskatchewan, Canada. In 1999, he joined the Department of Electrical and Computer Engineering, University of Alberta, Canada, where he is a Full Professor. Since 2016, he has served in various leadership roles in the Department. Currently, he is an Associate Dean (Research Operations) at the Faculty of Engineering. His research interests include artificial intelligence and energy systems. He developed a number of innovative solutions in the areas of renewable energy systems, smart grids, wireless sensor networks, and environmental sensing, monitoring, and modeling.